Retrieving the Complex Transmission Matrix of a Multimode Fiber by Machine Learning for 3D Beam Shaping

Benjamin Gobé, Jérémy Saucourt, Maksym Shpakovych, David Helbert, Agnès Desfarges-Berthelemot, and Vincent Kermene

***Abstract*—There is an upward trend in using multimode fiber for an increasing number of applications such as optical telecommunication, endoscopic imaging or laser beam shaping, which require knowledge of the fiber characteristics. In this paper, we propose a new method for learning the complex transmission matrix of a multimode fiber from a set of speckled output patterns without interferometric setup. In a first step, our method finds a model to predict the intensity pattern of a coherent beam at the distal end of the multimode fiber. In a second step, this model is improved by using some additional intensity images in the far field, resulting in the prediction of the actual 3D complex field leaving the multimode fiber, without the use of a reference beam. Our two-step method was validated numerically and experimentally with a standard 50 μm-core diameter step-index fiber guiding up to 140 LP modes at 1064 nm. Experimentally, using the validation set, we obtain a similarity between predicted and true speckle images at fiber output of 99.2% and 98.5% respectively in the near field and far field, proving the accuracy of the retrieved complex transmission matrix. Finally, we successfully demonstrated projection of images simultaneously in two planes as proof of complex field shaping.**

***Index Terms*—Complex transmission matrix, deformable mirror, machine learning, multimode fiber, referenceless method.**

I. Introduction

IN THE recent years, performance improvements of spatial light modulators (SLM) or digital micro-mirror devices (DMD), namely larger number of pixels, higher frequency modulation, better stability and power handling have led to a renewed interest in multimode fibers (MMF). Even if the coherent field from a MMF appears to have a random structure (speckle), this is actually a deterministic distribution, resulting from a linear transform of the excited field described by modes propagation in the fiber. It is therefore possible to control the interference pattern at the MMF output by pre-compensating the wavefront of the laser field seeding the fiber with a SLM. This coherent control has opened up new perspectives for MMFs [1] and expanded their fields of application, such as in optical telecommunications [2], [3], [4], bio-imaging [5], [6], [7], spectroscopy [8], quantum signal processing [9] or laser source [10]. To shape a laser beam from a MMF, there are four main types of processes: digital phase-conjugation [11], adaptive control in a feedback loop [12], neural networks (NN) for image propagation [13], [14], [15], or modal decomposition [16] and transmission matrix (TM) measurement [17], [18]. The first two approaches have mainly demonstrated their ability to focus the field at the fiber output. In [13], [15], in order to predict the input phase-map required for a desired image at the MMF output, the authors need to learn at least two sub-NN, one for the forward propagation through MMF and the other for the backward description. The TM of the MMF describes the relationship between the coherent field on the SLM and the field leaving the fiber (from the actuators of the SLM to the pixels of the camera imaging the end facet of the MMF). Then, using the inverted TM, one can theoretically synthetize on demand at the fiber output any complex field that is a linear combination of the fiber modes. Usually, an interferometric setup with a reference beam retrieves the phase of the output beam to build the TM [5]. This method is complex to set-up and particularly difficult to implement when measuring the TM of a long MMF. Thus, different works already proposed to measure this TM without any reference beam, only from a set of output intensity patterns obtained with different input wavefronts. They require solving a set of non-linear equations that links the field displayed on the SLM to the corresponding output intensity pattern. Very recent publications have proposed optimization algorithms based on specific gradient descent [19], [20] or on alternating projection [21] to improve the accuracy of the recovered TM, evaluated by the focusing quality through the MMF. Despite significant enhancement of the focusing parameter, the experimental results show a large discrepancy with the expected theoretical value. These experiments highlight the sensitivity of the algorithms to noisy data, degrading the TM quality. Moreover, the TM learnt thanks to a set of speckled patterns at the MMF output can only predict intensity patterns in this target plane, like focused beam for instance. As the TM's rows are independently optimized, there exists an unknown and random phase bias between them. Very recently, J. Zhong et al. [22] used a set of additional measurements taken in a Fresnel

Manuscript received 22 December 2023; revised 5 February 2024 and 26 February 2024; accepted 28 February 2024. Date of publication 5 March 2024; date of current version 8 July 2024. This work was supported in part by Région Nouvelle Aquitaine under Grant AAPR2020-2019-8128410 and in part by Agence AMIES under Grant UAR3458 Labex. *(Corresponding author: Vincent Kermene.)*

The authors are with the XLIM Research Institute, UMR 7252 CNRS/ University of Limoges, F-87000 Limoges, France (e-mail: benjamin.gobe@xlim.fr; jeremy.saucourt@xlim.fr; maksym.shpakovych@xlim.fr; david.helbert@xlim.fr; agnes.desfarges-berthelemot@xlim.fr; vincent.kermene@xlim.fr).

Color versions of one or more figures in this article are available at https://doi.org/10.1109/JLT.2024.3373689.

Digital Object Identifier 10.1109/JLT.2024.3373689

plane of the fiber output to recover and correct the phase bias. Thus, they demonstrated focusing in different planes at the fiber exit after phase bias correction. Recovery of the complex TM from intensity-only images was demonstrated in 2022 thanks to a transformer NN that managed a few number of modes (∼5 LP modes) [16]. In the present work, we report a new reference-less method based on machine learning that provides a high fidelity TM of a highly multimode fiber without any phase bias. It offers the ability to deliver controlled 3D coherent fields at the fiber distal end instead of 2D intensity patterns with remaining phase errors as commonly reported. The performances of the method are evaluated through speckle correlations between experimental measurements and images in two specific planes (output fiber plane and its corresponding far field) given by the predicted TM.

II. MMF Transmission Matrix Recovery by Machine Learning

Our objective was to optimize by a supervised machine learning approach the components of the TM that models the propagation of a coherent field in a linear regime, through a MMF. In the context of controlling the emission of a MMF, the transmission matrix $A \in \mathbb{C}^{m\times n}$ connects the field $x \in \mathbb{C}^n$ at the input of the MMF (proximal end), to the field $y \in \mathbb{C}^m$ at the output (distal end). Each 2D complex field x and y is reshaped as vector to match the relation $y = Ax$. Without any reference beam in the setup, the basic data available to train the matrix A are the complex field x controlled by a SLM and the related intensity $|y|^2$ on a CMOS camera at the fiber output. In our experiment, as the SLM is a segmented deformable mirror which modulates the incident wavefront, only $\mathrm{Arg}(x)$ is varied to create the dataset, $|x|$ is provided by the Gaussian amplitude of the incident beam onto the SLM. With these data, we aimed first at optimizing a model A_{Int}, which provides intensity predictions $|y_{Int}|^2$ at the distal end of the MMF from the relationship: $|y_{Int}|^2 = |A_{Int}x|^2$ with $\mathrm{Arg}(x) \in [-\pi, \pi[^n$ and $|y_{Int}|^2 \in \mathbb{R}_*^{+m}$. However, this single intensity constraint does not allow retrieving the true matrix A. Indeed, any additional phase bias $\psi \in [-\pi; +\pi[^m$ between the rows of A_{Int} produces the same output intensity pattern, as shown by the following equality:

$$|y_{Int}|^2 = |A_{Int}x|^2 = |\mathrm{diag}\left(\exp\left(j\psi\right)\right) A_{Int}x|^2 \qquad (1)$$

with the operator $\mathrm{diag}(\cdot)$ a square diagonal matrix from a vector argument.

This results in accurate intensity but random output phase prediction, as it was also shown in [22]. To remove the phase ambiguity between the rows of matrix A_{Int} and then correct the phase bias ψ, we propose to use a few additional measurements $|z|^2$ in the Fourier plane of the distal field y which are sensitive to the phase of y. In this second step, we learnt the bias phase ψ so that the ground truth $|z|$ matches $|\mathrm{FT}(\mathrm{diag}(\exp(j\psi))\ A_{Int}x)|$ where FT is a 2D Fourier transform operation. Then, the trained transmission matrix A_ψ was built from both recovered matrix A_{Int} and vector ψ:

$$A_\psi = \mathrm{diag}\left(\exp\left(j\psi\right)\right) A_{Int} \qquad (2)$$

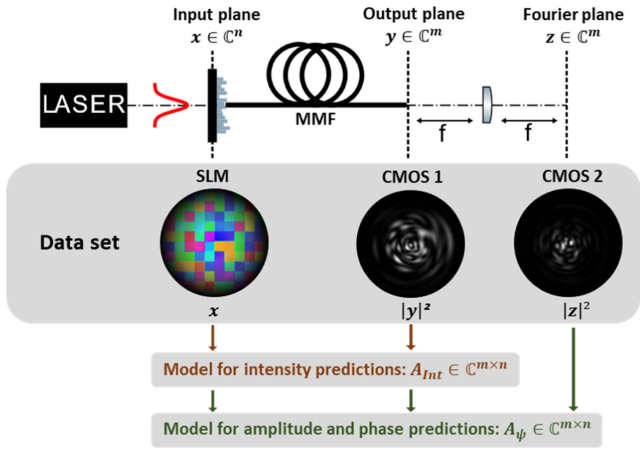

Fig. 1. Conceptual representation of the MMF transmission matrix measurement, highlighting the data set which seeds the machine learning process in both main steps.

To learn A_{Int}, we used a dataset $D = \{X, |Y|^2\}$ obtained by applying N random phase maps on the SLM ($X \in \mathbb{C}^{n\times N}$), and by measuring the corresponding intensities ($|Y|^2 \in \mathbb{R}_*^{+m\times N}$) on the camera CMOS1 (see Fig. 1). This dataset fed a mini-batch gradient descent algorithm that minimized the cost function $\mathcal{L}_1(|Y_{Int}|^2, |Y|^2)$ (3) with Adaptive Moment Estimation (ADAM) with respect to the parameters A_{Int} [23].

$$\mathcal{L}_1\left(|Y_{Int}|^2, |Y|^2\right) = \frac{1}{mN}\sum_{j=1}^{N}\sum_{i=1}^{m}\left(|Y_{Int}|^2{}_{ij} - |Y|^2_{ij}\right)^2 \qquad (3)$$

Algorithm 1 describes the optimization process. The components of A_{Int} are trained to minimize the distance between the measured physical intensity $|Y|^2$ and the predicted ones $|Y_{Int}|^2 = |A_{Int}X|^2$. We built a dataset of small size $D_\mathcal{F} = \{X_\mathcal{F}, |Z_\mathcal{F}|^2\}$ made of $N_\mathcal{F} \ll N$ additional random phase maps on the SLM ($X_\mathcal{F} \in \mathbb{C}^{n\times N_\mathcal{F}}$), and the corresponding intensities measured on a second camera (CMOS2) in the Fourier plane $\mathcal{F}$ of the output of the MMF ($|Z_\mathcal{F}|^2 \in \mathbb{R}_*^{+m\times N_\mathcal{F}}$). It fed a gradient descent algorithm which minimizes the cost function $\mathcal{L}_2(|\mathrm{FT}(Y_\psi)|, |Z_\mathcal{F}|)$ (4) with ADAM using the dataset $D_\mathcal{F}$.

$$\mathcal{L}_2\left(|\mathrm{FT}\left(Y_\psi\right)|, |Z_\mathcal{F}|\right) = 1 - \Gamma\left(|\mathrm{FT}\left(Y_\psi\right)|, |Z_\mathcal{F}|\right) \qquad (4)$$

where $Y_\psi = A_\psi X$, A_ψ verifies (2), and ψ is the parameter to be optimized. The function Γ stands for the Pearson correlation coefficient, generally expressed as:

$$\Gamma\ (a,\ b) = \frac{\sum\left(|\mathrm{vec}\ (a)| - \overline{|\mathrm{vec}\ (a)|}\right)\cdot\left(|\mathrm{vec}\ (b)| - \overline{|\mathrm{vec}\ (b)|}\right)}{\sqrt{\sum\left(|\mathrm{vec}\ (a)| - \overline{|\mathrm{vec}\ (a)|}\right)^2}\cdot\sqrt{\sum\left(|\mathrm{vec}\ (b)| - \overline{|\mathrm{vec}\ (b)|}\right)^2}} \qquad (5)$$

where a and b are generic real- or complex-valued n-dimensional tensors, $\mathrm{vec}(\cdot)$ is a matrix vectorization, and $\overline{(\cdot)}$ is the arithmetic

Algorithm 1: Mini-batch Gradient Descent Algorithm to Learn A_{Int} that Predicts the Intensity Pattern $|y_{Int}|^2$.

Hyperparameters: Batch size $B \in \mathbb{N}$, learning rate $\eta \in \mathbb{R}_*^+$, learning rate decay $\tau \in]0, 1]$
Inputs: Loss function $\mathcal{L}_1$, phase modulated complex field $X \in \mathbb{C}^{n\times N}$, measurement matrix $|Y|^2 \in \mathbb{R}_*^{+^{m\times N}}$
Output: Trained weight matrix $A_{Int} \in \mathbb{C}^{m\times n}$

1. Initialize weight matrix with random initial weights $A_{Int} \in \mathbb{C}^{m\times n}$, learning rate η
2. Randomly shuffle the dataset D
3. Split the dataset D into a training set D^t and a validation set D^v
4. Repeat for $e = [1, \ldots, N_E]$ epochs:
   a. Randomly shuffle the training set D^t
   b. Repeat for the $b = [1, \ldots, N_B^t]$ mini-batches of the training set:
      i. Get the b^{th} mini-batch from the training set: $D^{t,b} = \{X^{t,b}, |Y^{t,b}|^2\}$
      ii. Evaluate the loss function: $\mathcal{L}_1(|A_{Int}X^{t,b}|^2, |Y^{t,b}|^2)$
      iii. Compute the gradient matrix: $\nabla_{A_{Int}}\mathcal{L}_1$
      iv. Update the weights matrix using ADAM update formula: $A_{Int} \leftarrow \text{ADAM}(A_{Int}, \eta, \nabla_{A_{Int}}\mathcal{L}_1)$
   c. Evaluate the loss function $\mathcal{L}_1$ on the validation set

Algorithm 2: Gradient Descent Algorithm to Learn the Phase Correction ψ and Get the Complex Transmission Matrix A_ψ.

Hyperparameters: learning rate $\eta \in \mathbb{R}_*^+$
Inputs: Learnt matrix $A_{Int} \in \mathbb{C}^{m\times n}$, loss function $\mathcal{L}_2$, phase modulated complex field $X_\mathcal{F} \in \mathbb{C}^{n\times N_\mathcal{F}}$, Fourier intensity measurements $|Z_\mathcal{F}|^2 \in \mathbb{R}_*^{+^{m\times N_\mathcal{F}}}$
Output: Correction vector $\psi \in [-\pi, +\pi[^m$

1. Initialize correction vector matrix with random initial weights $\psi \in [-\pi, +\pi]^m$
2. Repeat for $k = [1, \ldots, K]$ epochs:
   a. Evaluate the loss function: $\mathcal{L}_2(|FT(A_\psi X_\mathcal{F})|, |Z_\mathcal{F}|)$
   b. Compute the gradient vector: $\nabla_\psi\mathcal{L}_2$
   c. Update the correction vector using ADAM update formula: $\psi \leftarrow \text{ADAM}(\psi, \eta, \nabla_\psi\mathcal{L}_2)$

mean. In the case of loss function $\mathcal{L}_2$, this metric compares the correlation between the Fourier measurement matrix $|Z_\mathcal{F}|$, and the prediction $|\text{FT}(Y_\psi)|$.

In Algorithm 2, the components of the phase bias ψ were trained to minimize the error between the Fourier measurements $|Z_\mathcal{F}|$, and the predicted Fourier measurements $|\text{FT}(\text{diag}(\exp(j\psi))A_{Int}X_\mathcal{F})|$. Matrix A_{Int} was finally corrected with the phase vector ψ to optimize the transmission matrix A_ψ to be close to the true matrix A. One could then predict the complex optical field at the output of the MMF from the learnt

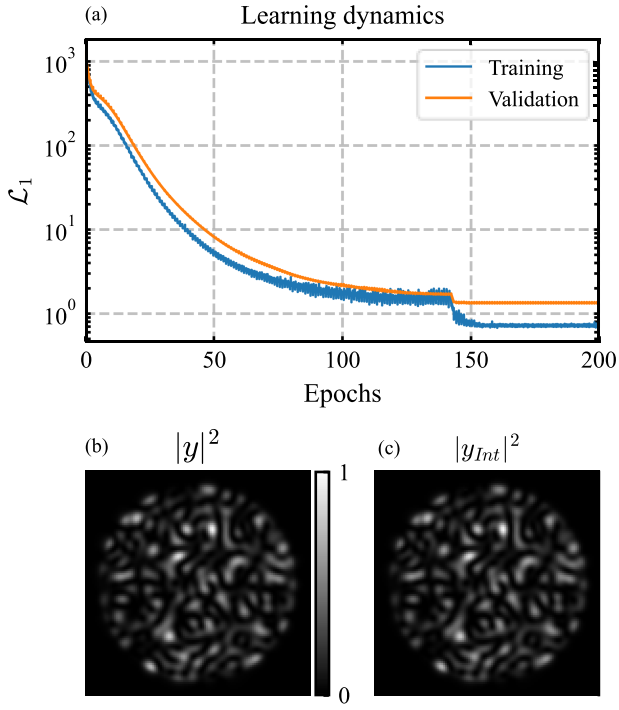

Fig. 2. (a) Learning dynamics as a function of epochs. Convergence is reached in about 150 epochs with a learning rate starting at 0.05. (b)–(c) One example of ground truth and predicted near field intensities.

matrix A_ψ. In practice, when considering an experimental setup, the TM includes the aberrations of the imaging systems at both sides of the fiber from the SLM to the detection planes.

III. Numerical Validation

The performance of this novel TM measurement method without any reference beam was first assessed with synthetic data. In the whole paper, we consider a standard step index MMF with a 50 μm-core diameter and a 0.22-numerical aperture, guiding up to 140 LP modes per polarization at 1064 nm. The datasets $D = \{X, |Y|^2\}$ and $D_\mathcal{F} = \{X_\mathcal{F}, |Z_\mathcal{F}|^2\}$ feeding the machine learning based Algorithms 1 and 2 were built with an arbitrary but realistic transmission matrix A**.** It described the propagation of an input Gaussian beam, from the SLM to the planes of the cameras CMOS1 and CMOS2, through the MMF. The incident wavefront was shaped by the SLM with a squared arrangement of n macro-actuators to form an input reduced vector $x \in \mathbb{C}^{\boldsymbol{n}}$.

To consider the inherent experimental detection noise, we added random values (Gaussian distribution) obtained from experimental data to the modeled intensities $|Y|^2$ and $|Z|^2$. We validated our machine learning approach for $n = 132$ macro-actuators, close to the number of LP modes. The computation spatial grid was 256x256 pixels in all the computed planes (both fiber ends and Fourier plane $\mathcal{F}$). Fig. 2(a) shows the learning curve of the matrix A_{Int} from Algorithm 1 using a number N^t of measurements in the training set that is 15 times the number n of actuators ($\gamma = \frac{N^t}{n} = 15$).

This curve represents the value of the loss function $\mathcal{L}_1$ for the training (solid curve) and the validation (dotted curve) sets as a function of epoch number. The decrease of the validation

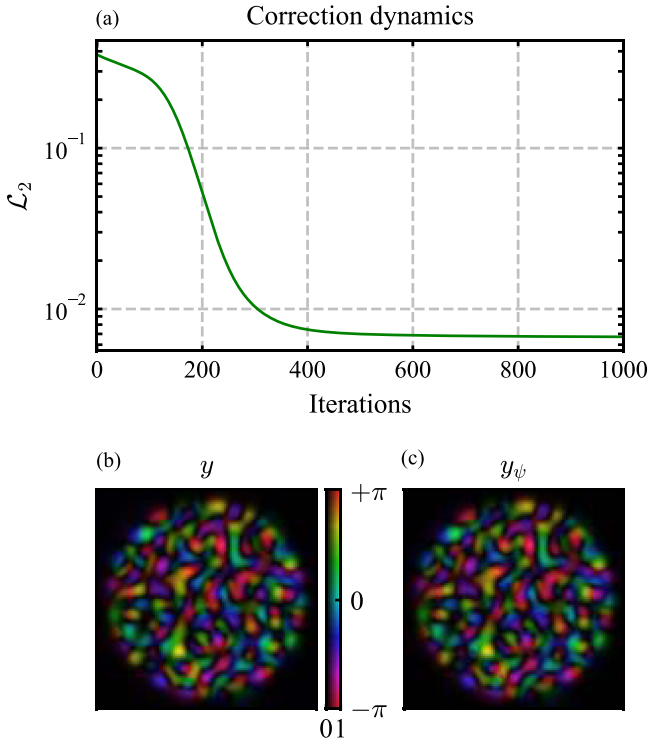

Fig. 3. (a) Optimization curve of Algorithm 2. Convergence is reached after about 700 iterations. (b)–(c) Example of ground truth and predicted complex near fields. Amplitude is encoded as brightness, and phase is encoded as hue.

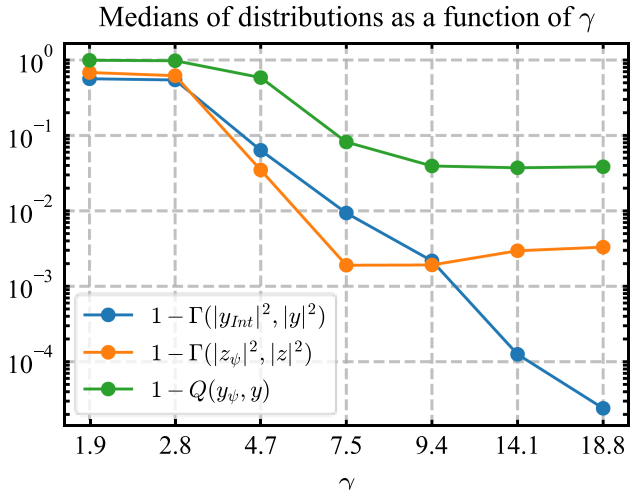

Fig. 4. Median of the metric distributions as a function of the ratio $\gamma = \mathrm{N^t}/\mathrm{n}$. Blue: Pearson correlation coefficient between the predicted and ground truth near field intensities. Orange: Pearson correlation coefficient between the predicted and ground truth far field intensities. Green: Quality factor between the predicted and ground truth complex near fields.

curve $\mathcal{L}_1$ is monotonic, and the distance with the training curve is constant, indicating that there is no overfitting. This training was run using a mini-batch size $B = 32$. Changing the mini-batch size did not significantly affect this learning curve, except for the time it requires. Indeed, higher mini-batch size reduces the computation time due to better parallelization. Fig. 2(b) and (c) highlights the similarity of an example of predicted intensity speckle $|y_{Int}|^2 = |A_{Int}x|^2$ with the true one $|y|^2$, x and $y \in D^v$ (validation dataset). The value of the Pearson correlation coefficient $\Gamma(|y_{Int}|^2, |y|^2)$ in this example reaches 99.99% and reveals the high fidelity of the computed model for intensity predictions. The whole validation dataset provides pictures with the same quality (see Fig. 2).

After this step, we improved the learnt model to get the phase-corrected transmission matrix A_ψ and predict the amplitude and phase of any optical field at the MMF distal end, knowing the input field x. We used the second dataset $D_\mathcal{F}$ with only 20 additional measurements in Fourier plane $\mathcal{F}$ to compute the A_ψ with the Algorithm 2. In Fig. 3(a), the loss function $\mathcal{L}_2$ converges to a low value (which corresponds to a high Pearson correlation coefficient), proving the efficiency of our two-step method. On Fig. 3(b) and (c), we compared the complex fields at the MMF distal end with and without phase correction ψ for an arbitrary x of the validation dataset ($x \in D^v$). One can observe the high fidelity of the predicted field after phase correction with the true one in amplitude and phase. Those results provide a first validation of our machine learning-based method.

More accurately, the performance of the learnt and phase-corrected matrix A_ψ was assessed using 1000 random draws within the validation set as a function of the ratio $\gamma = N^t/n$. We analyzed the distribution of three metrics: the MMF output intensity predictions $\Gamma(|y_\psi|^2, |y|^2)$, the Fourier intensity predictions $\Gamma(|\mathrm{FT}(y_\psi)|^2, |z|^2)$, and the MMF output complex field predictions $Q(y_\psi, y)$. This last quality factor is a normalized cross-correlation defined as follows:

$$Q\left(y_\psi, y\right) = \left(\frac{\sum_{i=1}^{m} |y_i \cdot y_{\psi i}{}^*|}{\sum_{i=1}^{m} |y_i| \cdot |y_{\psi i}|}\right)^2 \tag{6}$$

This quality factor quantifies the similarities of complex fields in amplitude and phase. Let us note that it can be computed in this numerical study but cannot be estimated with experimental data. Fig. 4 shows that for $\gamma \geq 10$, our method leads to excellent predictions. The intensity matching $\Gamma(|y_\psi|^2, |y|^2)$ at the MMF distal end was higher than 99.9%. As a first assessment of the quality of the phase correction, the similarity $\Gamma(|\mathrm{FT}(y_\psi)|^2, |z|^2)$ at the Fourier plane $\mathcal{F}$ was also excellent (higher than 99%). This leads to a very high quality $Q(y_\psi, y)$ of the overall complex field prediction, of about 95%.

We numerically tested our TM measurement method increasing the number of fiber modes up to 1000 LP modes. We maintained the number of actuators equal to the number of modes, $\gamma = 15$ and an image sampling with 256x256 pixels in the near and far fields. These simulations showed no degradation, the prediction efficiency is identical with a Q factor close to 96%. It is worth noting that the size of speckle grains decreases with the increase of modes number which means at some point increasing the number of samples in each near field and far field image. More modes would require a longer training time since, as the image size increases, so does the dimension of the transfer matrix.

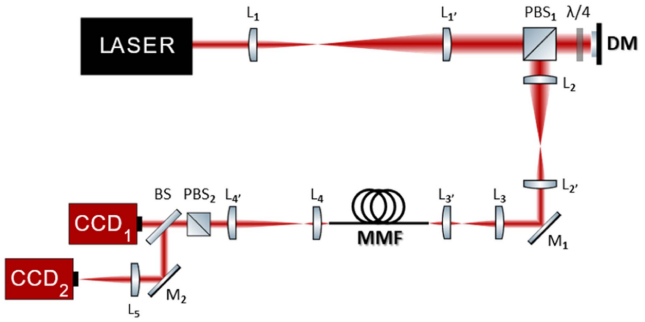

Fig. 5. Schematic of the experimental setup. The deformable mirror (DM) shapes the wavefront of the laser beam. It is imaged on the proximal facet of the MMF. The near field and far field from the distal facet of the MMF are imaged on CMOS cameras 1 & 2 respectively. Magnifications of the four afocal systems: $\frac{L_1'}{L_1} = 7.5$, $\frac{L_2'}{L_2} = \frac{1}{6}$, $\frac{L_3'}{L_3} = \frac{1}{40}$, $\frac{L_4'}{L_4} = 15.9$, L_5: $f_5 = 60$ mm, M mirror, PBS: Polarizing beam splitter.

IV. Transmission Matrix Measurements With Experimental Data

The experimental setup is schematically depicted on Fig. 5. The laser source was a distributed feedback laser diode operating in the CW regime at 1064 nm (QDLaser QLD1061). The MMF was the same standard step index fiber as the one used previously for the simulations (50/125 μm core/clad diameters, 0.22 numerical aperture, 1.5 meter-long, 140 LP modes/polarization). The laser beam, linearly polarized, with a Gaussian profile, was reflected onto a deformable mirror DM (Boston Micromachines Corporation, Kilo-CS-0.6-SLM), before seeding the MMF. The couple polarizing beam splitter (PBS) and quarter-wave plate (λ/4) is used to illuminate the DM in normal incidence with minimal losses. The incident beam fully covered the DM.

The DM shaped the beam wavefront of the signal with a matrix of n macro-actuators, which were made up of several elementary actuators. For the experiment, the number of macro-actuators was $n = 120$. The macro-actuators are made of 3x3 elementary actuators (12 macro-actuators per dimension distributed on a square mesh but on an overall round area). A couple of afocal systems imaged the DM plane onto the proximal facet of the MMF. At the other end of the fiber, an afocal system imaged the output near field on a CMOS camera (CMOS1) while an optical system displayed the far field of the output beam on a second CMOS camera (CMOS2). Both cameras provided 16-bit images (ThorCam CS2100) of size 256x256 pixels and 512x512 pixels (CMOS1 and CMOS2 respectively). Only the vertical polarization of the output beam was considered by positioning a polarizing beam splitter (PBS_2) between the fiber output and the cameras. A dataset of 1900 phase maps and related near field images was acquired at the low frequency of 11Hz, limited by the in/out access of the non-triggered camera and DM devices. This dataset was split into a training set with 1800 couples of data (15 times the number of macro-actuators) to learn the matrix A_{Int} and a validation set with the remaining 100 couples of data. Fig. 6(a) shows the convergence of the learning curve, which required about 150 epochs to converge with a 32-mini batch size and a learning rate starting at 0.05. The Pearson correlation

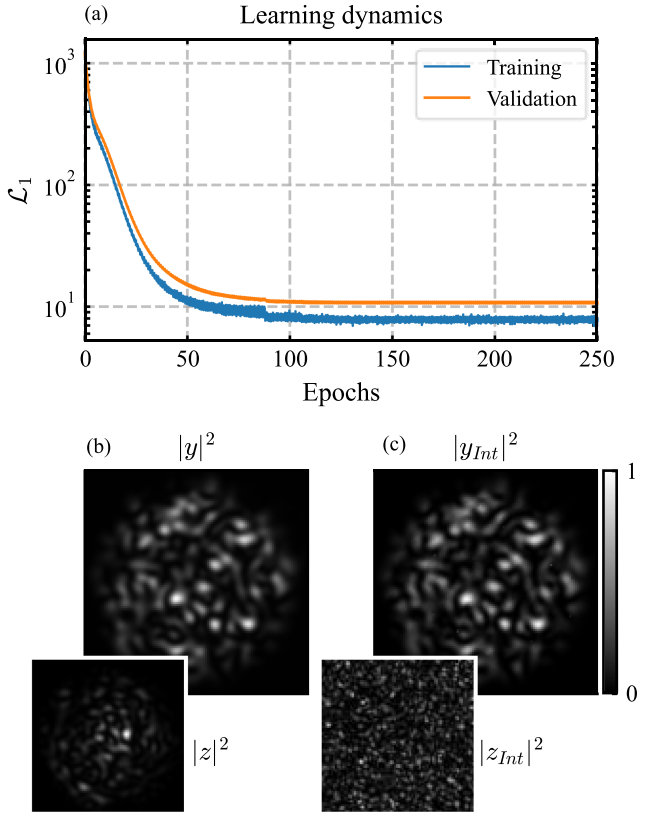

Fig. 6. Experimental data–(a) Learning dynamics as a function of epochs. Convergence is reached in about 150 epochs with 32-mini batch size and a learning rate starting at 0.05. It lasts about 200s with our Pytorch implementation using a laptop computer with a NVIDIA RTX A1000 4GB GPU and an Intel i7-12700H 2.30 GHz CPU. (b)–(c) Experimental and predicted near field intensities. Insets show the corresponding experimental and predicted far field intensities.

coefficient $\Gamma(|y|^2, |y_{Int}|^2)$ between experimental and predicted images from this dataset reached an average value higher than 99%.

These results confirm those of the numerical study: the model A_{Int} of the MMF that we retrieved by machine learning predicted intensity patterns almost identical to the intensity patterns produced by the fiber under test. Fig. 6(b) and (c) show an example of experimental and predicted near field intensities at the distal end of the MMF. The corresponding far field intensities are shown in the insets. As mentioned previously, the phase of the predicted field y_{Int} was biased. After this first step, y_{Int} exhibits in the Fourier plane an unrealistic number of fine speckle grains (inset of the Fig. 6(c)) due to the pixel-to-pixel random phase of y_{Int} predicted by the A_{Int}model, compared to the true Fourier image (inset of the Fig. 6(b)).

In a second step, as it was performed in the numerical validation, we recorded a testing dataset of 200 couples of near field and far field intensity patterns ($|y_{\mathcal{F}}|^2$ and $|z_{\mathcal{F}}|^2$), and their relative phase maps $x_{\mathcal{F}}$. Only 20 of these experimental images were used to compute the transmission matrix A_ψ by correcting the phase bias of the matrix A_{Int} previously retrieved. The optimization process with the Algorithm 2 required a few hundred iterations to

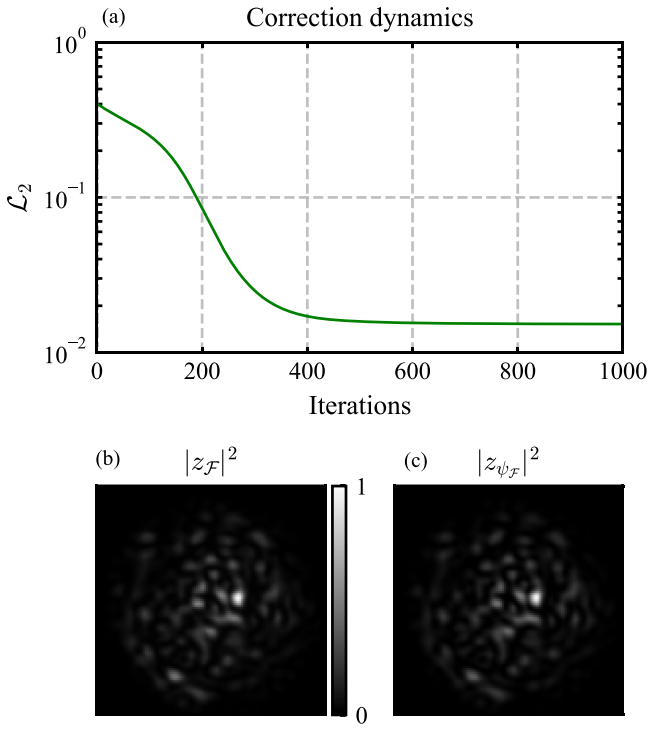

Fig. 7. Experimental data. (a) Optimization curve of Algorithm 2. Convergence is reached in about 700 iterations. (b)–(c) Example of experimental and predicted far field intensities.

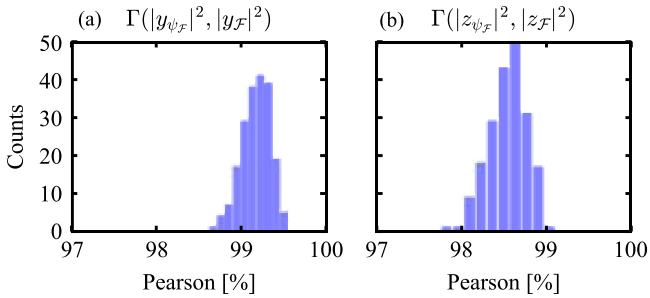

Fig. 8. Distribution of Pearson correlation coefficients between predicted and experimental intensities from the testing dataset in near field (a) and far field (b).

converge (Fig. 7(a)). Fig. 7(b) and (c) show an example of an experimentally measured far field and the corresponding predicted one by matrix A_ψ, highlighting the high similarity between the two. Finally, we quantified the quality of this new model A_ψ of the actual fiber complex TM on this test dataset. The Pearson correlation coefficient reached 99.2% on average in the near field (Fig. 8(a)) and 98.5% in the corresponding far field (Fig. 8(b)). These results are in line with the numerical simulations and confirm the accuracy of our referenceless two-step method to find the complex TM of a highly multimode fiber with a limited amount of data. Despite no specific precautions were taken to protect the fiber from environmental perturbations, the fidelity of the predicted speckle with respect to the experimental one was maintained during a few hours for which the TM did not change significantly.

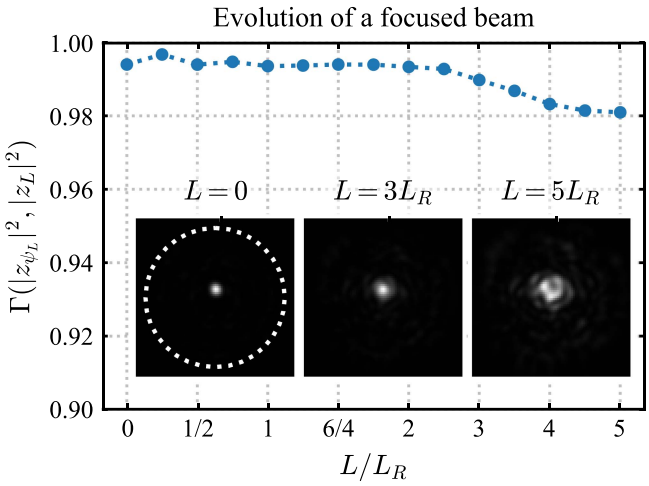

Fig. 9. Experimental data–example of focused beam at the fiber output, optimized from the experimental MT. Evolution of the Pearson correlation between the experimental images $|z_L|^2$ and the predicted ones $|z_{\psi_L}|^2$ along the propagation axis. L_R: Rayleigh length of the focused beam. Dashed white circle defines the fiber core.

Finally, we validated with two typical cases the ability of the measured complex TM to customize the MMF output beam in amplitude and phase. First, we computed the DM shape suited for focusing at the fiber end. The TM is usually inverted to calculate the input complex distribution relating to the output target. This method is not appropriate for our experimental set-up because the DM is a phase-only modulator with an amplitude constraint provided by the incident beam. Then we computed the phase to be applied to the DM using a gradient descent algorithm which reduces the deviation between the focused target and the output field given by the measured TM. Gradient descent is applied in a purely numerical loop including the measured TM ($\boldsymbol{A_\psi}$), learnt once, to find the DM phase vector $\hat{\phi} = \arg(x)$ that produces the target intensity patterns $|\boldsymbol{z_{L_i}}|^2$ at the distance $\boldsymbol{L_i}$ (ith target plane) from the MMF output. The phase vector is initialized to random or flat wavefront. The loss function is the sum of the Pearson correlation coefficients ($\boldsymbol{\Gamma}$) from the predicted amplitude $|\mathcal{F}\boldsymbol{r}_{\boldsymbol{L_i}}(\boldsymbol{A_\psi}(|\boldsymbol{x}|e^{j\phi}))|$in each plane i, and the target amplitude $|\boldsymbol{z_{L_i}}|$ in the respective plane:

$$\hat{\phi} = \min_{\phi \in [-\pi, +\pi[^n} \sum_{i=1}^{k} 1 - \Gamma\left(\left|\mathcal{F}r_{L_i}\left(A_\psi\left(|x|\, e^{j\phi}\right)\right)\right|, |z_{L_i}|\right)$$

$\mathcal{F}r_{L_i}$ is the Fresnel Transform for a propagation length L_i and k is the number of target planes (2 planes in the case of the Fig. 10). ADAM optimizer is used, with a constant learning rate value of 0.1 converging in about 50 iterations. Then, the optimized phase vector ϕ is applied on the DM. We assessed the 3D shaping by recording images in several output planes from the distal end of the fiber (plane of focusing) to 5 times the Rayleigh length (7.2 μm) of the focused beam (1/e^2 diameter = 3.1 μm). In addition, we compared these experimental data to the intensity distributions from the measured TM (Fig. 9). We quantified the fidelity between predictions and experiments with

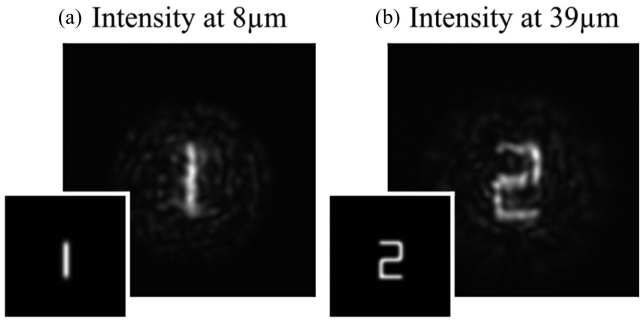

Fig. 10. Experimental data–examples of digit images display simultaneously in two different planes at 8 μm and 39 μm from the fiber distal end, obtained with a single optimized input phase map. Insets: Target digits.

the evolution of the 2D Pearson coefficient which is higher than 98% all along the beam propagation.

Then, to highlight the fact that our method fully characterizes the system in amplitude and phase, we investigated 3D shaping by performing image projections through MMF in two planes at the same time. This work extends the results of [14], [15] in which the authors demonstrated image projection at the distal end only, where the experimental data were recorded. Using the same optimization process as for focusing, we found the best input phase vector to target simultaneously two different arbitrary images in two planes at the fiber exit. Fig. 10 shows that the targeted digits 1 and 2 respectively at 8 μm and 39 μm distance planes from the fiber output are properly displayed. It has to be noted that these target planes are different from the fiber distal end plane where the data were recorded to learn the transmission matrix. These performances can only be reached if the true complex TM is retrieved: when the phase of the TM has been corrected in the second step of our process.

V. Conclusion

We propose a new method to measure the complex TM of a multimode fiber without interferometric setup nor reference beam. This method only requires a set of input fields structured by a deformable mirror and their corresponding output intensity images to predict this complex TM with a two-step machine learning approach. The first step consists in training a model A_{Int} that predicts intensity beam profiles at the fiber distal end, with a small number of training data (only 15 times the number of actuators of the deformable mirror). In a second step, no more than 20 additional Fourier patterns of the output beams are necessary to compute the actual complex TM A_{ψ} of the MMF. We numerically and experimentally demonstrated that our two-step method properly predicts the complex field at the distal end of a highly MMF, contrarily to previously reported machine learning based methods that only control the intensity profile of the output beam. In our study, we measured the TM of a 50/125 core/clad step-index fiber of 0.22 numerical aperture guiding 140 LP modes per polarization at 1064 nm, using a deformable mirror of 120 actuators. The convergence of the two algorithms (learning of model A_{Int} and phase bias correction step to get A_{ψ}) is reached in about 150 epochs with 32-mini batch size and 700 iterations respectively. Experimentally, the predicted intensity image and its corresponding far field reached a degree of similarity close to an excellent 99% with the true image on average. In comparison with other machine learning based methods, this is the first demonstration to the best of our knowledge, of highly MMF's true TM recovery from intensity-only measurements. The simplicity of the approach is an undeniable advantage from a practical point of view over more conventional techniques, which require a reference wave and a computational method for extracting the phase of the field at the fiber output. In addition to the high performance of intensity pattern predictions in both near field and far field with the measured TM, we use it to perform 3D shaping at the fiber output. In particular, we investigated the extend of previous demonstrations on image projection. As proof of principle, we experimentally demonstrated the delivery of two images in two different planes simultaneously, different from the fiber distal end where the data were recorded to learn the TM. These results pave the way to transmission through MMF of more information-rich images using the axial dimension. It is worth noting that a more complete characterization of the fiber can be obtained by measuring the TM at both orthogonal polarizations in the same way as described in this article. The actual modal TM of the MMF can also be deduced from the measured TM, knowing the guided modes of the fiber [24]. Finally, the principle of the technique is not limited to transmission through optical fibers since it is independent of the type of the crossed disturbing medium. In particular, it is also suitable to measure the TM of any random medium like a diffuser. These features are of particular interest in many applications such as beam shaping for surface treatments, motionless scanning, 3D photo-polymerization or to create optical tweezers in bioengineering.

Acknowledgment

For the purpose of Open Access, a CC-BY public copyright licence has been applied by the authors to the present document and will be applied to all subsequent versions up to the Author Accepted Manuscript arising from this submission.

References

[1] H. Cao et al., "Controlling light propagation in multimode fibers for imaging, spectroscopy, and beyond," *Adv. Opt. Photon.*, vol. 15, pp. 524–612, 2023.
[2] D. Richardson et al., "Space-division multiplexing in optical fibres," *Nature Photon.*, vol. 7, pp. 354–362, 2013.
[3] B. J. Puttnam et al., "Space-division multiplexing for optical fiber communications," *Optica*, vol. 8, pp. 1186–1203, 2021.
[4] S. Rothe et al., "Securing data in multimode fibers by exploiting mode-dependent light propagation effects," *Research*, vol. 6, 2023, Art. no. 0065, doi: 10.34133/research.006.
[5] T. Čižmár and K. Dholakia, "Shaping the light transmission through a multimode optical fibre: Complex transformation analysis and applications in biophotonics," *Opt. Exp.*, vol. 19, pp. 18871–18884, 2011.
[6] B. Lochocki et al., "Epi-fluorescence imaging of the human brain through a multimode fiber," *Appl. Phys. Lett. Photon.*, vol. 7, no. 7, 2022, Art. no. 071301.
[7] Z. Liu et al., "All-fiber high-speed image detection enabled by deep learning," *Nature Commun.*, vol. 13, no. 1, pp. 1–8, 2022, doi: 10.1038/s41467-022-29178-8.
[8] B. Redding and H. Cao, "Using a multimode fiber as a high-resolution, low-loss spectrometer," *Opt. Lett.*, vol. 37, pp. 3384–3386, 2012.

[9] G. B. Xavier and G. Lima, "Quantum information processing with space-division multiplexing optical fibres," *Commun. Phys.*, vol. 3, 2020, Art. no. 9.
[10] R. Florentin et al., "Shaping the light amplified in a multimode fiber," *Light: Sci. Appl.*, vol. 6, 2017, Art. no. e16208.
[11] I. N. Papadopoulos et al., "Focusing and scanning light through a multimode optical fiber using digital phase conjugation," *Opt. Exp.*, vol. 20, pp. 10583–10590, 2012.
[12] R. N. Mahalati et al., "Adaptive control of input field to achieve desired output intensity profile in multimode fiber with random mode coupling," *Opt. Exp.*, vol. 20, pp. 14321–14337, 2012.
[13] N. Borhani et al., "Learning to see through multimode fibers," *Optica*, vol. 5, pp. 960–966, 2018.
[14] B. Rahmani et al., "Actor neural networks for the robust control of partially measured nonlinear systems showcased for image propagation through diffuse media," *Nature Mach. Intell.*, vol. 2, no. 7, pp. 403–410, 2020.
[15] I. Wang et al., "Multimode fiber-based greyscale image projector enabled by neural networks with high generalization ability," *Opt. Exp.*, vol. 31, no. 3, 2023, Art. no. 4839.
[16] Q. Zhang et al., "Learning the matrix of few-mode fibers for high-fidelity spatial mode transmission," *Appl. Phys. Lett. Photon.*, vol. 7, no. 6, Jun. 2022, Art. no. 066104.
[17] J. Carpenter et al., "110x110 optical mode transfer matrix inversion," *Opt. Exp.*, vol. 22, pp. 96–101, 2014.
[18] R. Florentin, V. Kermene, A. Desfarges-Berthelemot, and A. Barthelemy, "Fast transmission matrix measurement of a multimode optical fiber with common path reference," *IEEE Photon. J.*, vol. 10, no. 5, Oct. 2018, Art. no. 7104706.
[19] G. Huang et al., "Retrieving the optical transmission matrix of a multimode fiber using the extended Kalman filter," *Opt. Exp.*, vol. 28, pp. 9487–9500, 2020.
[20] S. Cheng, T. Zhong, and P. Lai, "Non-convex optimization for retrieving the complex transmission matrix of a multimode fiber," in *Proc. IEEE Region 10 Conf.*, 2022, pp. 1–5.
[21] G. Huang et al., "Generalizing the Gerchberg–Saxton algorithm for retrieving complex optical transmission matrices," *Photon. Res.*, vol. 9, pp. 34–42, 2021.
[22] J. Zhong et al., "Efficient reference-less transmission matrix retrieval for a multimode fiber using fast Fourier transform," *Adv. Photon. Nexus*, 2023, Art. no. 5056007.
[23] D. P. Kingma and J. Ba, "Adam: A method for stochastic optimization," in *Proc. Int. Conf. Learn. Representations*, 2015.
[24] M. Plöschner et al., "Seeing through chaos in multimode fibres," *Nature Photon.*, vol. 9, pp. 529–535, 2015.